Research article

In silico and *in vivo* analysis reveal impact of c-Myc tag in FMC63 scFv-CD19 protein interface and CAR-T cell efficacy

Ana Julia Ferreira Lima [a,b,1], Karina Lobo Hajdu [c,1], Luiza Abdo [c], Leonardo Ribeiro Batista-Silva [c], Clara de Oliveira Andrade [c], Eduardo Mannarino Correia [c], Emmanuel Arthur Albuquerque Aragão [c], Martín Hernán Bonamino [c,d,*], Marcos Roberto Lourenzoni [a,**]

[a] *Research Group on Protein Engineering and Health Solutions (GEPeSS), Oswaldo Cruz Foundation Ceará (Fiocruz-CE), São José, Precabura, 61773–270 Eusébio, Ceará, Brazil*
[b] *Federal University of Ceará (UFC), Pici campus (Building 873), 60440-970 Fortaleza, Ceará, Brazil*
[c] *Cell and Gene Therapy Program, Research coordination – Brazilian National Cancer Institute, Rio de Janeiro, Brazil*
[d] *Vice - Presidency of Research and Biological Collections (VPPCB), Oswaldo Cruz Foundation (FIOCRUZ), Rio de Janeiro, Brazil*

ARTICLE INFO

ABSTRACT

Anti-CD19 CAR-T cell therapy represents a breakthrough in the treatment of B-cell malignancies, and it is expected that this therapy modality will soon cover a range of solid tumors as well. Therefore, a universal cheap and sensitive method to detect CAR expression is of foremost importance. One possibility is the use of epitope tags such as c-Myc, HA or FLAG tags attached to the CAR extracellular domain, however, it is important to determine whether these tags can influence binding of the CAR with its target molecule. Here, we conducted *in silico* structural modelling of an FMC63-based anti-CD19 single-chain variable fragment (scFv) with and without a c-Myc peptide tag added to the N-terminus portion and performed molecular dynamics simulation of the scFv with the CD19 target. We show that the c-Myc tag presence in the N-terminus portion does not affect the scFv's structural equilibrium and grants more stability to the scFv. However, intermolecular interaction potential (IIP) analysis reveals that the tag can approximate the complementarity-determining regions (CDRs) present in the scFv and cause steric impediment, potentially disturbing interaction with the CD19 protein. We then tested this possibility with CAR-T cells generated from human donors in a Nalm-6 leukemia model, showing that CAR-T cells with the c-Myc tag have overall worse antitumor activity, which was also observed when the tag was added to the C-terminus position. Ultimately, our results suggest that tag addition is an important aspect of CAR design and can influence CAR-T cell function, therefore its use should be carefully considered.

1. Introduction

Chimeric antigen receptor (CAR) T cell therapy has revolutionized the field of cancer immunotherapy. The original concept of the synthetic CAR molecule was to combine the specificity of an antibody with T cell effector functions, allowing redirection of T cell immune response against malignant cells expressing a specific membrane antigen [1]. Generally, the CAR consists of an extracellular target-binding domain connected *via* a hinge module and transmembrane domain to one or more intracellular signaling molecules [2]. The extracellular domain usually consists of a single chain variable fragment (scFv) composed of a variable light (VL) and variable heavy (VH) chain of a monoclonal antibody (mAb) joined by a linker [2]. The hinge connects the scFv to the transmembrane domain, which is responsible for anchoring the receptor to the T cell membrane and linking the extracellular to the intracellular domain [3]. Common intracellular signaling domains are the CD3ζ chain and costimulatory domains derived from CD28 or 41BB, which work together to provide full activation of the T cell [4]. CARs can be assembled by combining different versions of each of these structural determinant domains [5], and several improvements in CAR design have been tested in recent years with the aim of improving CAR target recognition and signaling [6].

The outstanding clinical success of CAR T cell therapy targeting the CD19 protein in patients with B-cell leukemias and lymphomas led to US Food and Drug Administration (FDA) approval of two CD19-specific CAR T cell products based on the FMC63 scFv in 2017, Kymriah and Yescarta [7,8]. CD19 has been chosen as an eligible target for CAR T cells in the treatment of B-cell malignancies because it is ubiquitously expressed throughout B-cell development and its expression is restricted to the B-cell lineage, being highly expressed in most B cell- derived tumors [9]. Since the first CAR-T cell therapy approvals, the number of clinical trials using different CAR constructs to recognize a variety of tumor antigens and even beyond solely targeting tumors is growing rapidly [10].

Despite these rapid advancements in CAR design and applications, there is still no universal detection method available to assess CAR expression on the surface of T cells [11]. Generally, CAR expression is detected *via* flow cytometry with fluorochrome-tagged antibodies or ligands that bind to the CAR extracellular domain, but antibodies targeting specific scFvs are costly [12–14]. A common cost-effective approach that can be applied to different CAR constructs is attaching a small epitope tag to the N-terminus or to the C-terminus region of the CAR extracellular domain. This method offers the possibility to detect, isolate and characterize CARs for which no specific antibodies are available [15]. Epitope tags like c-Myc, HA and FLAG are the most commonly used since their presence typically causes minimal to no effect on the target protein structure and function and due to wide availability of primary recognizing antibodies [16–19]. Our group and others have previously demonstrated the antitumor efficacy of anti-CD19 CAR-T cells containing an N-terminal c-Myc tag [20], however, to our knowledge, no previous study compared the same CAR construct with or without tag addition.

The c-Myc tag (EQKLISEEDL) is a short linear sequence of ten aminoacid residues derived from the c-Myc oncoprotein [21], which can be expressed in many types of eukaryotic and prokaryotic cells. This tag can be recognized by anti-c-Myc antibodies, such as the widely available 9E10 monoclonal antibody [15,22]. Due to these characteristics, the c-Myc tag has been extensively used in CAR studies [23–25]. A better understanding of if the c-Myc tag presence in the anti-CD19 scFv can potentially affect CD19 recognition and CAR function will allow improvements in the development and design of new CARs.

In this study we first modeled an FMC63-based scFv with the c-Myc tag in the N-terminus position interacting with the target protein and used Molecular Dynamics (MD) simulation to provide detailed information about interface formation between the scFv (with and without c-Myc tag) and CD19 [26,27]. Next, we compared antitumor efficacy of anti-CD19 CAR-T cells with or without the N-terminus c-Myc tag in an *in vivo* B-cell leukemia model, showing that the tag can negatively impact anti-tumor activity. To better understand whether this effect was specific to the tag in the N-terminus position, we also assessed the effect of a C-terminus c-Myc tag presence in the same CAR design *in vivo* and found similar results. Overall, our results suggest that epitope tags can interfere with CAR-T cell function, and therefore other detection approaches such as fluorescent reporters or independent membrane reporters (such as the dNGFR reporter) might prove more suitable to avoid undesirable effects [28,29]. By combining *in silico* modelling and functional CAR-T cell assays, this study provides a better understanding of the impact of epitope tag addition to scFvs and highlights the importance of thoughtful positioning of peptide tags in novel CAR designs.

2. Materials and methods

2.1. Molecular modeling

2.1.1. Construction of scFv and c-Myc-scFv models
The scFv tridimensional (3D) model of the FMC63 mAb was modeled using the multiple template modeling protocol of Modeller 9.20 program [30]. Five protein structures were chosen as a template, whose

sequences have homology > 59% (PDB code 3ESU, 3ESV, 3ET9, 3AUV, 6TCS). A flexible glycine/serine linker $(G_4S)_3$ was inserted between the VL C-terminus and the VH N-terminus. The best model out of 250 generated 3D models was chosen based on the DOPE score [31]. The best model was subjected to MD simulation to ensure the refinement of the 3D structure in aqueous solution.

To build the c-Myc-scFv 3D model, two linear structures of the c-Myc tag that were forming a complex with the anti-c-Myc antibody 9E10 Fab fragment (PDB code 2OR9) were added to the scFv VL domain N-terminus, using the PyMol 1.8 program [32].

2.1.2. Construction of CD19 model
The missing loops in the CD19 structure (PDB code 6AL5) were modeled since they are not present in the structure due to diffuse electron density. The missing residues homology modeling was performed in the Modeller 9.20 program [30] through missing residues modeling protocol. The original CD19 structure with some residues sequence modeled was used as a template for the comparative model construction.

2.2. Molecular docking

Molecular Docking studies were performed to identify the interface region between scFv and CD19 (scFv-CD19) and c-Myc-scFv and CD19 (c-Myc-scFv-CD19) using the HADDOCK 2.2 webserver [33]. HADDOCK has a flexible docking approach, which can be guided by incorporating experimental or bioinformatics data [34,35]. Among the information that can be added to guide the docking is the definition of the residues that are important for protein-protein interface formation, which is denominated as active residues. The scFv active residues defined in the docking were the CDRs (Table S1 - supplementary material) and CD19 active residues were defined according to Table S2, which shows the CD19 residues that are important in recognition by this scFv, according to the literature [36–38]. The CD19 structure was kept fixed during docking. Docking results show the formation of the scFv-CD19 and c-Myc-scFv-CD19 complexes and the results were grouped into 6 and 10 clusters, respectively. The scFv-CD19 and c-Myc-scFv-CD19 complexes named two MD simulation systems. The selection of the docking results was performed by evaluating the HADDOCK score, cluster size, root-mean-square deviations (RMSD) and z-score.

2.3. Molecular dynamics simulation

The molecular dynamics (MD) simulations were performed using GROMACS 2018.3 software [39] using CHARMM36 [40] force field to describe the atomic interactions. The structures obtained through homology modeling (scFv, c-Myc-scFv, CD19) and molecular docking (scFv-CD19 and c-Myc-scFv-CD19) were inserted in a simulation box with water molecules to form MD simulation systems. Each assembled system and the parameters used are described in Table S3. The atomic coordinates of each structure were submitted to the H+ + server [41] to verify histidine protonation status at a pH of 7.4 (physiological pH). Then the structures were placed in a box filled with TIP3P water molecules [42]. The protein bond lengths were controlled using the LINCS [43,44] algorithm, and those of water were controlled using SHAKE [45] algorithm. The interactions between unbound atoms (van der Waals and Coulomb) were evaluated at a cut-off radius of 1.3 nm and corrections for electrostatic interactions were calculated using the Particle Mesh Ewald (PME) method [46].

The energy minimization of the systems was performed using the steepest descent integrator [47] to optimize the geometry of the protein. In the thermalization and trajectory production phases, combinations of MD simulations were used in the NVT and NPT ensembles (Table S4). The temperature was controlled by the V-rescale thermostat [48] while the system pressure was controlled with the Berendsen barostat [49] in thermalization, and Parrinello-Rahman [50] in trajectory acquisition. Pressure was controlled at 1 atm, at a temperature of 310 K, and the

systems were neutralized with Na$^+$ and Cl$^-$ ions at a physiological concentration of 0.150 M. The integrator used to integrate the equations of motion was the leap-frog [51]. The short and successive thermalizations steps were carried out in the NVT and NPT ensemble at 310 K. The thermalization protocol of each system is detailed in Table S4. Trajectory acquisition phase was carried out in the NPT ensemble with a dt = 2 fs, where the coordinates were recorded every 100 ps.

2.3.1. Simulation conditions of scFv, c-Myc-scFv and CD19

The structures obtained through molecular modeling (scFv, c-Myc-scFv, and CD19) were submitted to MD simulation during 700, 700, and 300 ns, respectively. CD19 structure in water was simulated in the first 100 ns with simulated annealing to obtain the minimum energy state of the modeled loops, leaving only them free to move. More detailed parameters of the MD of each system are listed in Table S4.

2.3.2. Simulation conditions of scFv-CD19 and c-Myc-scFv-CD19

Each structure described in the previous section, which was previously simulated in water, was subjected to molecular docking to obtain the interface structures (scFv-CD19 and c-Myc-scFv-CD19) and to form the systems to submit them to the MD simulation, which was performed in triplicates (n1, n2, and n3). More detailed parameters of the MD of each system are listed in Table S4.

2.3.3. Simulation conditions of scFv-c-Myc

To compare how the tag position added to the scFv can influence the interface formation, we decided to perform 700 ns of MD simulations of the scFv with the c-Myc tag added to the C-terminus (scFv-c-Myc system). The information about this system is listed in Tables S3 and S4.

2.3.4. Simulation conditions of CAR-C-Myc

To analyze if the c-Myc tag in the C-terminus position impacts CAR structure, we built the CAR extracellular and transmembrane domains with the c-Myc tag between the scFv and hinge domains (CAR-C-Myc system) [52,53]. This system was subject to MD simulation for 400 ns. More information about this system is listed in Tables S3 and S4.

2.4. Trajectory analysis

The root-mean-square deviations (RMSD), intermolecular interaction potential (IIP), and binding free energy (ΔG_{bind}) analysis were built using GROMACS 2018.3 package [39]. All graphs were plotted using the Origin 8.0® program. The gmx rms program was used to calculate the RMSD of carbon α atoms (Cα) of the protein structures collected in the trajectory over time after overlapping to the MD initial structure. The IIP was calculated using the gmx energy, through the sum of long-range (electrostatic) and short-range (Lennard-Jones) potentials within a cutoff radius of 1.3 nm. The IIP expresses the interaction potential between unbounded atoms, for example, between the group of atoms of c-Myc and CDRs, scFv and CD19, and c-Myc-scFv and CD19. The ΔG_{bind} was determined for the interaction between scFv-CD19 and c-Myc-scFv-CD19, using the MM-PBSA method [54] (by the g_mmpbsa program). The distance between the first and last Cα atoms of the c-Myc (Glu243 and Leu262, respectively) and the first and last Cα atoms of the hinge structure (Thr263 and Asp307, respectively) was calculated using the gmx distance program.

2.5. Plasmids

The original 19BBz sequence [55] encoding an anti-CD19 CAR with FMC63-derived scFv [56], a 41BB costimulatory domain and the CD3ζ chain, was provided by Dr Dario Campana (St Jude Children Research Hospital, Memphis, TN). The sequence was codon-optimized and a c-Myc peptide tag (EQKLISEEDL-EQKLISEEDL) was added between the CD8α signal peptide and the scFv light chain (VL) (N-terminus position, named 19BBz.N-Myc) or between the scFv VH and the hinge domain

(C-terminus position, named 19BBz.C-Myc) (Fig. S6A). This sequence was synthesized by Genscript (Piscataway, NJ) and cloned in the Sleeping Beauty transposon vector pT3 (provided by Dr Richard Morgan, NIH) with *Age*I and *Not*I restriction enzymes. Synthesis and cloning of 19BBz without the c-Myc tag in the pT3 vector was done by Epoch Life Science, Inc. The plasmid pCMV-SB100x encoding a hyperactive form of the Sleeping Beauty transposase (SB100x) [57] was kindly provided by Dr Sang Won Han (Federal University of São Paulo -UNIFESP, Brazil).

2.6. Cell lines

Human CD19 + B-cell ALL cell lines RS4;11 and Nalm-6 were modified to express green fluorescent protein (GFP) and firefly luciferase (fluc) using lentiviral vectors and selected by cell sorting. Cells were maintained in a humidified incubator at 37 °C with 5% CO$_2$ atmosphere in RPMI-1640 media (Gibco, CA) supplemented with 10% fetal bovine serum (FBS), 2 mM L-Glutamine (Gibco) plus 100 U/mL penicillin and 100 μg/mL streptomycin (pen/strep, Gibco). To generate CD19lo Nalm-6, the gRNA sequence used for Crispr-Cas9-mediated knockout was CTGTGCTGCAGTGCCTCAA. Ribonucleoproteins (RNPs) were formed by incubation of 90 pmol of gRNA and 30 pmol of Alt-R S.p. Cas9 Nuclease V3 (Integrated DNA Technologies, Inc) 1 × 10^6 Nalm-6 GFP+Luc+ cells were centrifuged at 100 g for 10 min at room temperature and resuspended in 100 μl of 1SM electroporation buffer [58]. Cells were transferred to a 0.2 cm cuvette (Mirus Biotech®, Madison, WI) and electroporated in a Lonza® Nucleofector® II device with the X-001 pulse program. After electroporation, cells were resuspended in RPMI medium with 20% FBS without pen/strep and placed in a 24-well plate. Cells were sorted according to CD19-APC MFI expression on a MoFlo Astrios EQ (Beckman Coulter).

2.7. Primary cells and CAR-T cell generation

The use of samples from healthy blood donors was approved by the Brazilian National Cancer Institute (INCA)'s Ethics Committee review board. To generate CAR-T cells, leukocyte reduction filters (RS - Haemonetics) were obtained from blood bags from healthy donors at the blood bank of INCA after signing an informed consent approved by the Ethics Committee. After washing the filter with 80 mL of Phosphate Buffered Saline (PBS), PBMCs were isolated by density gradient centrifugation with Ficoll-Hypaque-1077 (Sigma Aldrich) for 25 min at 400 g with slow acceleration and break off. Cells were collected from the buffy coat and washed three times with PBS before counting. Cells were electroporated using the program U-14 and 3 × 10^7 cells per 0.2 cm cuvette in 100 μl of 1SM buffer. Mock controls were electroporated with 1 μg of SB100X plasmid encoding the SB transposase, while 19BBz, 19BBz.N-myc and 19BBz.C-Myc groups received 1 μg of SB100X + 20 μg of the plasmid encoding the CAR. After electroporation, cells were carefully resuspended in 1 mL of RPMI medium supplemented with 20% FBS, 2 mM L-glutamine, 10 mM HEPES (Sigma), 1 mM pyruvate (Gibco) and 50 U/mL human IL-2 (Proleukin, Zodiac) without pen/strep and transferred to a 6-well plate already containing 1 mL of medium/well. Cells were activated with T Cell TransAct CD3/CD28 beads (Miltenyi Biotec, Germany) at 1:200 concentration 2 h after electroporation. In the next day, the media supplemented as described and 100 U/mL penicillin + 100 μg/mL streptomycin was added to each well. Cells were maintained at 37 °C 5% CO$_2$ during the 8-day expansion, and received more complete media when acidification occurred.

2.8. Cytotoxicity assays

2.8.1. 4-hour lysis assay

The cytotoxicity assay was based on the original methodology described by Neri et al. [59]. Briefly, Nalm-6 and RS4;11 target cells were incubated with 15 μM Calcein-AM (Thermo Fisher Scientific, Burlington, CAN) (10^6 cells /mL) in complete RPMI media for 30 min at

37 °C with periodic agitation. Cells were then washed twice in complete media, counted, and resuspended to a final concentration of 5×10^3 cells/50 μl media. Effector cells were counted and plated at a serial dilution ranging from 50:1 to 0.78:1 effector: target (E/T) ratio in 100 μl complete media on V-bottom 96-well plates in triplicates. Next, 50ul of media containing the target cells was added to each well. After 4 h of incubation at 37 °C and 5% CO_2, the plate was quickly spun down and 75 μl of supernatant was harvested from each well. Calcein fluorescence was measured in a SpectraMax® iD3 microplate reader (Molecular Devices) with 485 ± 9 nm excitation filter and 530 ± 9 nm band-pass filter. Positive controls containing stained target cells + media with 2% Triton X-100 were added (maximum release, minimum 4 wells) and negative controls containing stained target cells in complete media (spontaneous release, minimum 4 wells). Lysis percentage was calculated based on replicate mean according to the formula: [(test release − spontaneous release)/ (maximum release − spontaneous release)] × 100.

2.8.2. Long lysis assay

The frequency of CAR$^+$ cells at day 8 of expansion was determined by flow cytometry, and total cell number was adjusted using Mock cells to have the same number of effector cells in all groups. Nalm-6 GFP+ cells were used as targets and added at 1:1 (3×10^4:3×10^4) and 0.5:1 ratio (1.5×10^4:30×10^4) (effector: target) in a final volume of 200 μl RPMI media in a U-bottom 96-well plate. After 48 h and 96 h, cells were harvested and stained with Fixable Viability Dye eFluor™ 780 (eBioscience, 65–0865-14). Killing activity of effector cells was determined by quantifying the number of live GFP$^+$ target cells. Negative controls with only target cells were included.

2.9. Cell staining and flow cytometry

Cells were stained for immunophenotyping 24 h after electroporation and at the end of T cell expansion on day 8. Briefly, cells were washed with PBS and incubated with previously tittered antibodies (Table S5) for 15–25 min at 4ºC. Next, cells were washed again with PBS and read in the cytometer the same day or fixed with paraformaldehyde 4%. For staining with the FITC-conjugated CD19 protein (CD19p-FITC), cells were incubated for 1 h with 10 ug/mL CD19p-FITC in 20 μl and washed twice, following manufacturer's instructions. All data was acquired in a FACS Canto II (BD Bioscience) and analyzed using FlowJo software v10.1 (Treestar Software, San Carlos, California, USA). Mock controls were used to define CAR+ gates and fluorescence minus one (FMO) controls were added for multicolor panels.

2.10. Xenograft mice model

Female NOD-SCID IL2R gamma null (NSG) mice originally purchased from the Jackson laboratories between eight to twelve-weeks old were kept at the Brazilian National Cancer Institute (INCA) animal facility with maximum 5 animals per cage at 12 h light: 12 h dark photoperiods, controlled temperature and free access to food and water. Animals were randomized between groups and all experimental procedures were performed in compliance with INCA's ethics committee approval. Experiments were non blinded, and no sample size calculation was performed. Mice were injected intravenously (i.v.) *via* the tail vein with 10^5 Nalm-6 GFP+Luc+ cells in 100 μl sterile PBS. After 48 h, animals received treatment with CAR-T lymphocytes. Before injection cells were counted, washed and resuspended in sterile PBS at a final volume of 100 μl per animal and injected i.v. *via* the tail vein. Mock controls received the same total cell number of treatment groups. CAR-T cell dose calculation was based on percentage of CAR+ cells on the day of injection.

Tumor burden was assessed by *in vivo* bioluminescence imaging on an IVIS Lumina XR (Caliper Life Sciences). Mice were injected intraperitoneally with 100 μl D-luciferin (75 mg/kg, GoldBio) and anesthetized with 4% isoflurane for induction + 2% isoflurane for

maintenance during image acquisition. Data was analyzed on Living Image Software v4.1 (Perkin Elmer). The time for euthanasia was based on disruption of animal welfare such as signs of pain, neurological symptoms and/or posterior limbic paralysis due to high tumor burden. A CO_2 chamber was used. The spleen and bone marrow were collected and analyzed by flow cytometry to detect GFP+ Nalm-6 tumor cells.

2.11. Data analysis

Data from *in vitro* and *in vivo* experiments was analyzed using GraphPad Prism version 8.0.1 (GraphPad, La Jolla, USA). We used Student's t test to compare means between two groups with or without pairing depending on the experiment (e.g same donor data was considered paired data). One-way analysis of variance (ANOVA) followed by Tukey's post-hoc was used to compare means of three or more groups. Survival data was analyzed using the log-rank test. A p-value < 0.05 was considered statistically significant and sample size is indicated in each figure legend.

3. Results

3.1. Evaluation of scFv, c-Myc-scFv and CD19 structures in aqueous solution

To better understand the potential impact of the c-Myc tag addition to the anti-CD19 scFv, we chose to simulate the scFv with the N-terminal c-Myc tag (referred here as c-Myc-scFv) as this is a commonly used position [25]. Root-mean-square deviation (RMSD) profiles allow analyzing the structural equilibrium of scFv alone and c-Myc-scFv in water during 700 ns of simulation (Fig. S1A, **B**). The scFv linker was disregarded from the RMSD analysis in both systems, as it presents flexible residues of glycine and serine, which leads to high RMSD fluctuations. In the scFv system (Fig. S1A), the RMSD of VL-VH and VH were similar and bigger than the RMSD of VL. This indicates that VL-VH movements can be associated to those of VH, because the VL presents small oscillations in the structure (RMSD of VL $\sim 0.10 \pm 0.01$ nm). After $\sim$250 ns, the scFv reached structural equilibrium (t_{eq}) and remained in equilibrium until the end of the simulation, presenting an average RMSDs of 0.16 ± 0.01 nm, 0.10 ± 0.01 nm, and 0.17 ± 0.01 nm for VL-VH, VL and VH respectively.

In the c-Myc-scFv system (Fig. S1C), the RMSD of c-Myc was $0{,}66 \pm 0{,}12$ nm, an average RMSD and deviation considered high, which is expected for a sequence of residues coupled to the N-terminus of the scFv and which is free to move (Fig. S1C) (Table S6). Consequently, the c-Myc was disregarded from the RMSD analysis focusing only on the structure of VL-VH. The RMSD of VL-VH and VH were similar and higher than the RMSD of VL (Fig. S1B), it is so similar for the scFv on the other system (Fig. S1A), including the average RMSD (Table S6).

Therefore, the similarities between the profiles and the RMSD averages between the c-Myc-scFv and scFv systems allow us to infer that there is no influence of c-Myc on the scFv structure. Additionally, we did not observe structural changes promoted by the tag addition in the VL-VH structure that could impact the interface formation with CD19.

The CD19 structure was monitored by calculating the RMSD during the last 300 ns of simulation (Fig. S1 **D**). The missing loops modeled in the CD19 structure proved to be quite flexible during the MD simulation. So, the RMSD analysis for CD19 was performed, disregarding the modeled loops presence. The RMSD profile for CD19 is at zero in the first 100 ns due to the structure of CD19 remaining constrained during the simulated annealing phase, a phase in which only the modeled loops were free to move in successive heating and cooling cycles, seeking to find more stable conformations of these loops. The average RMSD for CD19 throughout the simulation was 0.28 ± 0.03 nm (Table S6).

3.2. The c-Myc tag attached to the N-terminus influences the formation of the scFv/CD19 interface

An Intermolecular Interaction Potential (IIP) analysis between c-Myc and the scFv complementarity-determining regions (CDRs) was performed using a cutoff radius of 1.3 nm (Fig. 1**A**) to identify whether the c-Myc tag approaches this region in a way to interact attractively.

In the IIP profile (Fig. 1**A**), IIP < 0 kcal.mol^{-1} is observed during most of the simulation, meaning that there is an attractive interaction between c-Myc and the scFv CDRs. The profile oscillates in levels of ~ − 40 kcal.mol^{-1} with a clear transition to smaller IIP, reaching − 200 kcal mol^{-1}, denoting a more attractive interaction between c-Myc and the CDRs, indicating that c-Myc approaches the CDRs at some moments in the simulation. Therefore, we infer that depending on the relative position between the c-Myc tag and the CDRs, the presence of this tag can affect the interface formation with CD19. The IIP distribution histogram in Fig. 1**B** clearly shows distribution maxima at − 45.97 and − 92.25 kcal.mol^{-1}, with 41% of the time (Fig. 1**C**) c-Myc being in a conformation that allows potential attractive interaction below − 45.97 kcal.mol^{-1}.

Fig. 2 (**A-C**) shows the configurations, in 4 views, in instants of the simulations where the IIP are − 26.25, − 45.97, and − 92.25 kcal mol^{-1}, respectively. Notably, for the instants 369 ns (IIP = −45.97 kcal.mol^{-1}) and 361 ns (IIP = −92.95 kcal.mol^{-1}) (Fig. 2**B, and C**, respectively), it is seen that the tag is in an orientation that makes it difficult to approach for the formation of an interface with CD19. In view 4, in a frontal view of the CDRs, c-Myc is ahead of the CDRs for IIP of − 92.95 kcal.mol^{-1} (Figs. 2**C**) and − 45.97 kcal.mol^{-1} (Fig. 2**B**), showing that for these configurations, the IIP difference between the two configurations is due to closer approximation of c-Myc with CDR H2. However, in both configurations, c-Myc is positioned in front of the CDRs, which may prevent the scFv/CD19 interface formation.

3.3. Interface formation between scFv and CD19

Based on the most recent publications regarding the CD19 epitope recognized by the scFv derived from the antibody FMC63, the results obtained demonstrate the significant importance of the following CD19 residues: Leu97, Trp159, Arg163, Lys220, Gly221, and Pro222 which are comprised of three loops, called Loop 1, Loop 2 and Loop 3 (Table S2) [36–38]. But in the recent work by He et al. [38], Loop 2 and Loop 3 receive a different denomination, being called Loop 1 and Loop 2, respectively. When these residues were mutated, they caused a loss of interaction between FMC63 scFv and CD19 and were, therefore, considered key residues in this recognition between antibody-CD19 [36, 37]. Among the residues indicated as CD19 key for interaction with scFv, the main ones were chosen for the docking, being Arg163 of Loop 2 and all residues of Loop 3, except for Ser224, as it is more hidden in the structure of CD19 (Table S2).

The structures that were the most representative during each simulation (scFv, c-Myc-scFv, and CD19) were collected through cluster analysis to be used in the molecular docking. Furthermore, the c-Myc-scFv structure collected had the c-Myc far from the CDRs, presenting an IIP within the range between 0 and − 26 kcal.mol^{-1}, so this tag would not potentially interfere with the interface formation. The CD19 structure selected presented the key residues (Table S2) in the interaction with the scFv facing the region where the scFv would anchor. Fig. 3 shows the superimposed structures of the complexes scFv-CD19 and c-Myc-scFv-CD19 obtained by docking. Notably, in this orientation, the c-Myc addition to scFv does not interfere significantly with the interface formation between scFv and CD19.

3.4. Structure dynamics, molecular interaction and binding free energy of scFv and c-Myc-scFv in interface with CD19

The complexes obtained through the docking with c-Myc (c-Myc-scFv-CD19) and without c-Myc (scFv-CD19) were submitted to MD simulation for 1000 ns in triplicate (n1, n2, and n3). The structural variations of the scFv and CD19 were evaluated by RMSD profiles (Fig. S2). The RMSD profiles were generated disregarding the scFv linker, the c-Myc tag and the loops modeled on CD19, due to the known high conformational degree of freedom in these regions.

The RMSD profiles in Fig. S2 show that, in both scFv-CD19 and c-Myc-scFv-CD19 systems, VL-VH, VL, and VH domains maintain their
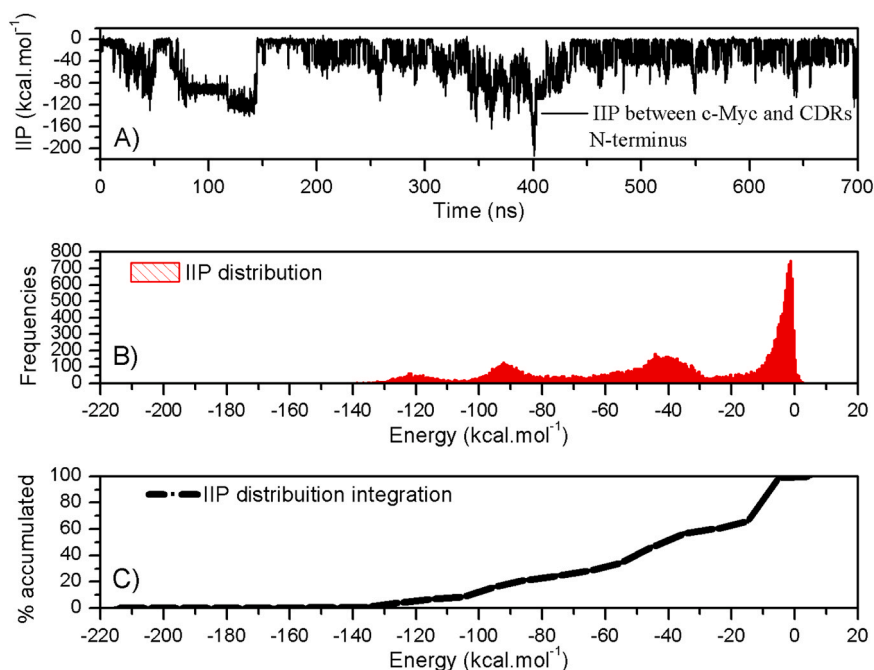

Fig. 1. IIP profiling between c-Myc and CDRs to determine when c-Myc potentially disrupts CD19 interfacing when placed at the scFv N-terminus. A) IIP profile between c-Myc and CDRs using a cutoff radius of 1.3 nm. **B)** Histogram of IIP distribution in relation to the observation of these values throughout the simulation. The values − 92.25, − 44.25 and − 26.25 are expressed in kcal.mol^{-1}. **C)** Accumulated percentage of IIP values throughout the simulation.

220 ns (-26.25 kcal.mol^{-1})   **369 ns** (-45.97 kcal.mol^{-1})   **361 ns** (-92.25 kcal.mol^{-1})
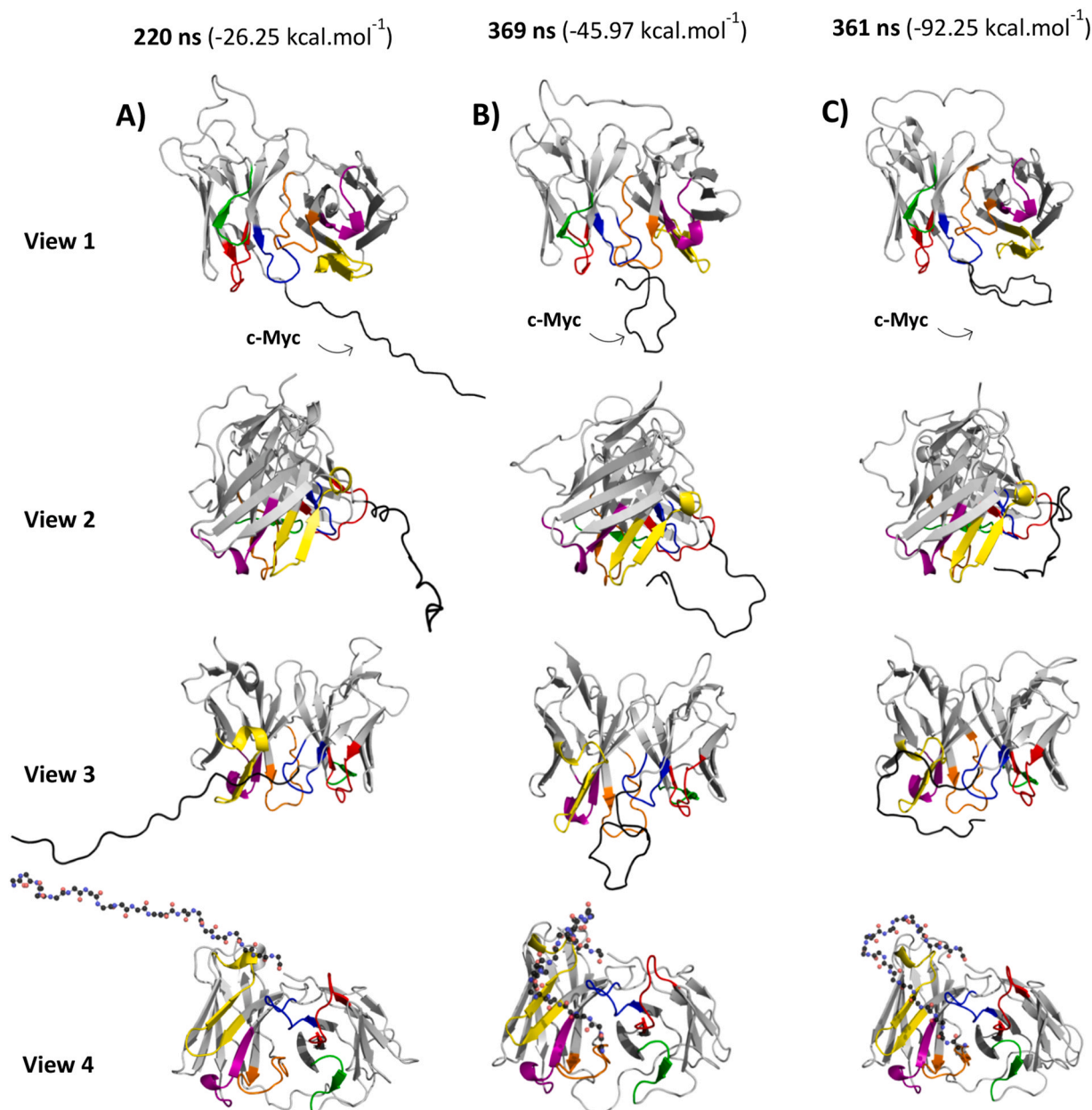

Fig. 2. Representation of c-Myc-scFv structures in cartoon collected at different simulation times to assess the relative position between c-Myc and CDRs in four views and relate to the IIP values observed at these times. A) Structure collected at 220 ns, which results of IIP was − 26.25 kcal.mol^{-1}. **B)** Structure collected at 369 ns, which results of IIP was − 45.97 kcal.mol-1. **C)** Structure collected at 361 ns, which results of IIP was − 92.25 kcal.mol-1. The c-Myc structure is identified in black, and the CDRs with colors refer to Table S1. CDR L1 (red), L2 (green), L3 (blue), H1 (purple), H2 (yellow), and H3 (orange). In view 4, c-Myc is identified in spheres, where the carbon atoms are represented in black, the oxygen atoms in red, and in blue the nitrogen atoms.

structure with variations in solution of 0.1–0.2 nm, which is expected for protein movement under the thermal effect of water [60]. Regarding the VL-VH and VH and VL domains, RMSD averages in scFv-CD19 system ranged between (0.13 and 0.14 ± 0.01 nm) for the VL-VH, and the domains VL (0.10 to 0.12 ± 0.01 nm), and VH (0.10 to 0.13 ± 0.01 nm) (Fig. S2 **A-C**). Comparing the RMSD profiles of the two systems, it is noted in c-Myc-scFv-CD19 system (Fig. S2 **D-F**) that VL gains structural stability in relation to scFv-CD19 system, as well as VL is slightly more stable than VH. Table 1 shows that in the c-Myc-scFv-CD19 system, the VL has a lower average RMSD in triplicates, which may infer that c-Myc helps to stabilize the VL structure when interfaced with CD19.

The RMSD for CD19, in the system scFv-CD19 (Fig. S2 **A-C**), oscillates over time above 0.3 nm, with a maximum amplitude of ∼ 0.475 nm at n1 (Fig. S2A). The peak in the profile with subsequent

reduction of RMSD denotes that there are movements in the structure of CD19 when interfaced with scFv. Since CD19 RMSD profiles show a significant increase before 100 ns, teq = 100 ns was considered for the average calculations for both systems. The average RMSD for CD19 ranges from 0.28 to 0.30 ± 0.02 nm and from 0.23 to 0.30 ± 0.02 nm in the scFv-CD19 and c-Myc-scFv-CD19 system respectively, indicating a subtle stability in CD19 in c-Myc-scFv-CD19 (Table 1). However, a plateau was observed in the RMSD profile in the c-Myc-scFv-CD19 system for ∼220 ns and returned to lower values (Fig. S2 **D**), configuring two apparent structural states. The RMSD profiles (Fig. S2 **E, F**) are quite similar, as are the average RMSD (Table 1).

The RMSD profiles for CD19 in the c-Myc-scFv-CD19 and scFv-CD19 systems and among the triplicates are quite similar (Fig. S2). The RMSD profiles oscillate over time with an average RMSD above ∼0.30 nm at
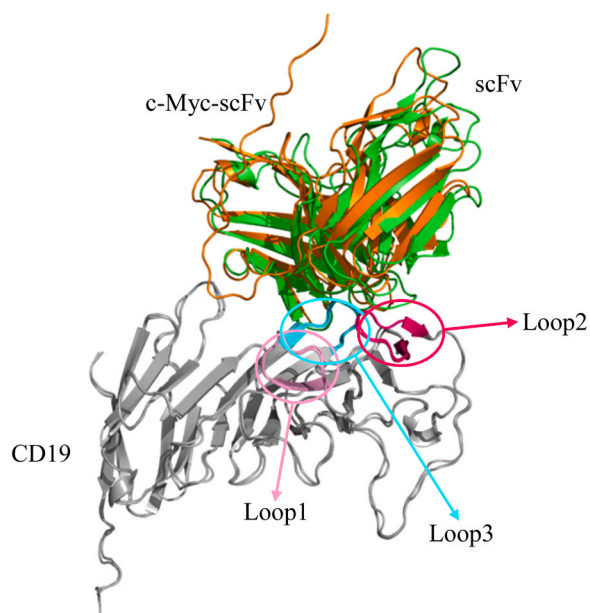
Fig. 3. Interface formation between scFv (with and without the N-terminus c-Myc) and CD19 obtained through docking results. 3D structures of the interface formation between scFv (green) and c-Myc-scFv (orange) with CD19 (grey) superimposed, identifying the loops corresponding to the antigenic epitope (Loop1: light pink; Loop2: dark pink; Loop3: cyan).

Table 1

Average RMSD data and deviations for domains: VL-VH, VL, VH, and CD19 of both systems (scFv-CD19 and c-Myc-scFv-CD19) for the three simulations n1, n2 and n3, calculated from the moment that structural equilibrium is reached, teq = 100 ns.

System		Average RMSD ± Deviation (nm)				teq (ns)
		VL-VH	**VL**	**VH**	**CD19**	
scFv-CD19	n1	0.13 ± 0.01	0.12 ± 0.01	0.10 ± 0.01	0.30 ± 0.02	100
	n2	0.14 ± 0.01	0.10 ± 0.01	0.13 ± 0.01	0.30 ± 0.02	100
	n3	0.13 ± 0.01	0.11 ± 0.01	0.11 ± 0.01	0.28 ± 0.02	100
c-Myc-scFv-CD19	n1	0.13 ± 0.01	0.08 ± 0.01	0.13 ± 0,01	0.25 ± 0.02	100
	n2	0.15 ± 0.01	0.09 ± 0.01	0.17 ± 0,01	0.23 ± 0.02	100
	n3	0.14 ± 0.01	0.09 ± 0.01	0.14 ± 0,01	0.28 ± 0.02	100

the end of MD (Table 1). The structure of CD19 contains many loops, including those that were discounted in the RMSD calculation. However, the profiles show rapid changes in RMSD that suggest movements in the loops. Likewise, the variation in the profiles of RMSDs ranging from ~4.5 nm and returning to the ~2–3 nm plateau suggests subtle structural changes at longer times.

Through IIP analysis between scFv CDRs and CD19, IIP values < 0 were observed in both scFv-CD19 and c-Myc-scFv-CD19 systems (Fig. S3). Thus, there is an attractive interaction between scFv and CD19. For the scFv-CD19, the simulations n1 and n2 (Fig. S3 **A and B**, respectively) presented similar profiles. The profiles oscillate in levels of ~ -140 kcal.mol^{-1} and are maintained throughout the simulation for n1 and n2 (-144.15 ± 37.54 kcal.mol^{-1} and -137.22 ± 26.38 kcal. mol^{-1}) (Table 2). In this sense, even with oscillations in the CD19 structure, the interface with scFv is maintained. Hence, the movements in CD19 are in regions that are not part of the interface, as they do not change the IIP at the same instants. However, in n3 (Fig. S3 **C**), there is

Table 2

Average IIP and deviations in kcal.mol^{-1}, calculated for the interaction between scFv and CD19 in the scFv-CD19 and c-Myc-scFv-CD19, for the three simulations n1, n2 and n3.

System	IIP (kcal.mol^{-1})		
	n1	**n2**	**n3**
scFv-CD19	-144.15 ± 37.54	-137.22 ± 26.38	-129.05 ± 43.00
c-Myc-scFv-CD19	-152.25 ± 33.04	-184.71 ± 33.28	-194.55 ± 35.95

an increase in the IIP at the end of MD simulation, denoting a severe reduction in the attraction between scFv and CD19. The average IIP between scFv-CD19 for the n3 system is -129.05 ± 43.00 kcal.mol^{-1}, greater than that for n1 and n2, as well as the deviation from the mean (Table 2). This suggests that the interface stability in n3 is more fragile.

On the system with c-Myc-scFv and CD19 interface, the IIP profiles in n1, n2 and n3 systems are quite similar (Fig. S3 **D-F**), with more negative IIP values being observed in n3. The average IIP is -152.25 ± 33.04 kcal.mol^{-1}, -184.71 ± 33.28 and -194.55 ± 35.95 kcal.mol^{-1}, for systems n1, n2 and n3 (Table 2). The profiles oscillate ~ -180 kcal.mol^{-1} at the end of MD simulation. It can be inferred that the c-Myc tag does not negatively interfere with the interface formed between scFv and CD19. Furthermore, the average IIPs are significantly lower in the c-Myc-scFv-CD19 system than scFv-CD19 (Table 2), revealing that c-Myc stabilizes the complex formed between scFv and CD19.

The results of the binding free energy by the MM-PBSA method are shown in Table 3. In the complex formed between c-Myc-scFv and CD19 the average ΔG_{bind} is negative (-71.71 ± 36.31 kcal.mol^{-1}) and lower than that observed between scFv and CD19 (-7.49 ± 27.20 kcal. mol^{-1}). Therefore, the predicted binding affinity is enhanced for the c-Myc-scFv-CD19 complex relative to the scFv-CD19. These data corroborate the IIP results that already indicated the presence of c-Myc as promoting a more stable binding between scFv and CD19.

3.5. The presence of the c-Myc tag does not influence CAR-T cell in vitro expansion and phenotype

To assess the potential impact of the c-Myc tag on CAR-T cell function, we generated anti-CD19 CAR-T cells from PBMC of healthy human donors using the Sleeping Beauty transposon system as previously described [54]. CAR-T cells with scFvs containing the N-terminus c-Myc tag (named 19BBz.N-Myc) or without c-Myc tag (19BBz) presented a similar percentage of CAR+ cells after expansion *in vitro* (Fig. 4**A**), ranging from 10–20% CAR+ cells on day 1 to 20–38% on day 8. We compared the mean fluorescence intensity (MFI) of CAR-T cells stained with a FITC-conjugated CD19 protein and did not observe a significant difference between groups (Fig. 4**B**, paired by same donors), suggesting that for the *in vitro* expansion based on anti-CD3/CD28 beads stimulation the c-Myc tag does not impact the outcome. Our expansion protocol with low-dose IL-2 resulted in CAR-T cells with mixed effector memory and central memory phenotype in both groups on day 8 (Fig. 4**C**) and favored the expansion of CD8 cells relative to CD4 cells (Fig. 4**D**). CAR-T cells showed moderate to high levels of surface activation/exhaustion

Table 3

Binding free energy ΔG (kcal.mol^{-1}) between scFv and c-Myc-scFv in interaction with CD19, in the scFv-CD19 and c-Myc-scFv-CD19 systems in triplicate. ΔG_{bind} is the average between triplicate n1, n2, and n3 MD simulations.

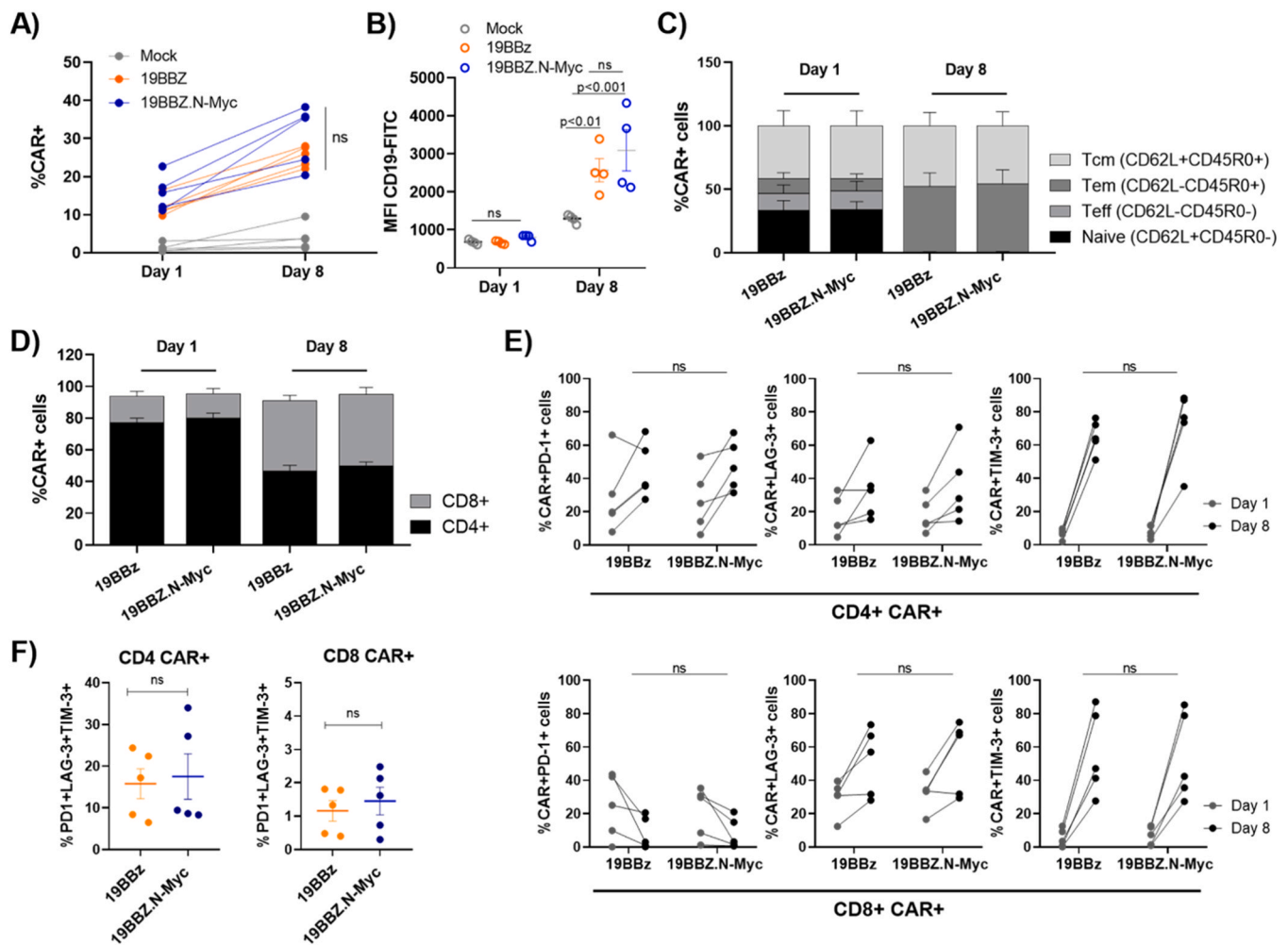| System	ΔG_{bind} n1	ΔG_{bind} n2	ΔG_{bind} n3	ΔG_{bind} (kcal. mol^{-1})
scFv-CD19	-4.74 ± 26.93	-12.72 ± 26.89	-5.01 ± 27.79	-7.49 ± 27.20
c-Myc-scFv-CD19	-76.85 ± 37.94	-81.90 ± 34.63	-56.39 ± 36.37	-71.71 ± 36.31

Fig. 4. Characterization of 19BBz and 19BBz.N-Myc CAR-T cells generated with the Sleeping Beauty system. PBMCs from healthy blood donors were electroporated with CAR plasmids and SB100X transposase and expanded with anti-CD3/CD28 transact + low-dose IL-2 for 8 days. Mock controls were electroporated only with SB100X transposase. Cells were stained with antibodies for characterization 24 h after electroporation and at the end of the expansion. **A)** Percentage of CAR+ cells in culture on day 1 and after 8 days of expansion detected by staining with FITC-conjugated CD19 protein. **B)** FITC-conjugated CD19 protein MFI after 1 h staining. **C)** Memory profile of CAR+ cells based on the expression of CD45R0 and CD62L, where naive cells are defined as CD45R0-CD62L+ , effector cells as CD45R0-CD62L-, effector memory cells as CD45R0 +CD62L- and central memory cells as CD45R0 +CD62L+ . **D)** Percentage of CAR+ CD4 and CD8 T cells on day 1 and day 8 of the expansion. **E)** Expression of activation and exhaustion markers PD-1, LAG-3, and TIM-3 on CD4 and CD8 CAR-T cells showing individual donors on days 1 and 8 and concomitant expression of all markers at the end of the expansion. **F)** Graphs show mean ± SEM of minimum 4 individual donors.

markers PD-1, LAG-3 and TIM-3, which increased by day 8 compared to day 1 (Fig. 4E-F). The exception was PD-1 expression on CD8 CAR-T cells, which was higher on day 1 compared to day 8, in line with a transient upregulation of PD-1 after T cell activation [20]. Altogether, our data from *in vitro* expansion of CAR-T cells with or without the c-Myc tag show that the tag does not influence CAR expression or activation, resulting in similar phenotypes and cell counts *in vitro*.

3.6. 19BBz cells perform better in vivo against CD19 + B-ALL Nalm-6 tumor cells compared to 19BBz.N-myc cells

We hypothesized that perhaps the influence of the c-Myc tag could occur during longer term interaction with the CD19 target, since our *in-silico* data shows that in certain moments the tag approximates the CDRs in the scFv, which could impact interface formation between the scFv and the CD19 protein. Furthermore, the *in vitro* expansion protocol used to expand the cells does not rely on CD19 engagement. To assess this question, we conducted *in vivo* experiments inoculating immunodeficient NSG mice with the CD19 + B-cell ALL cell line Nalm-6 modified to express GFP and firefly luciferase (Nalm-6 GFP+Luc+). We used CAR-T cells from the same donor to conduct both an *in vitro* 4-hour lysis assay

(Fig. 5A-B) and to treat mice bearing Nalm-6 tumor (Fig. 5 C). We saw no difference in cytotoxic activity of 19BBz and 19BBz.N-myc CAR-T cells when co-cultured for 4 h with Nalm-6 or RS4;11 CD19 + targets, indicating that activation thresholds to promote target killing are likely achieved with either CAR design (Fig. 5B). However, in a context of repeated exposure to leukemia such as the *in vivo* xenograft model, 19BBz CAR-T cells performed significantly better than 19BBz.N-myc in both doses tested - a lower dose of 0.7×10^6 CAR+ cells and a higher dose of 1.4×10^6 CAR+ cells (Fig. 5D-G)- indicating that it is possible to lower CAR-T cell doses to achieve the same effect *in vivo* when the c-Myc tag is not present.

We further tested the impact of the c-Myc tag using a limiting low dose of CAR-T cells in a second experiment with CD19low Nalm-6 GFP+Luc+ generated with CRISPR-Cas9. This CD19lo cell line had approximately a 40% decrease in CD19 MFI (Fig. S4 A), and we sought to assess if it could alter *in vivo* response when using a low-dose treatment. We injected 0.6×10^6 CAR+ cells (Fig. S4 B) in mice bearing Nalm-6 GFP+Luc+ CD19lo tumor and followed the tumor burden. Both 19BBz and 19BBz.N-myc still showed a significant response compared to untreated controls (Fig. S4 C-G), which can be seen both in survival gain (Fig. S4 F) and decreased percentage of GFP+ tumor cells in the spleen
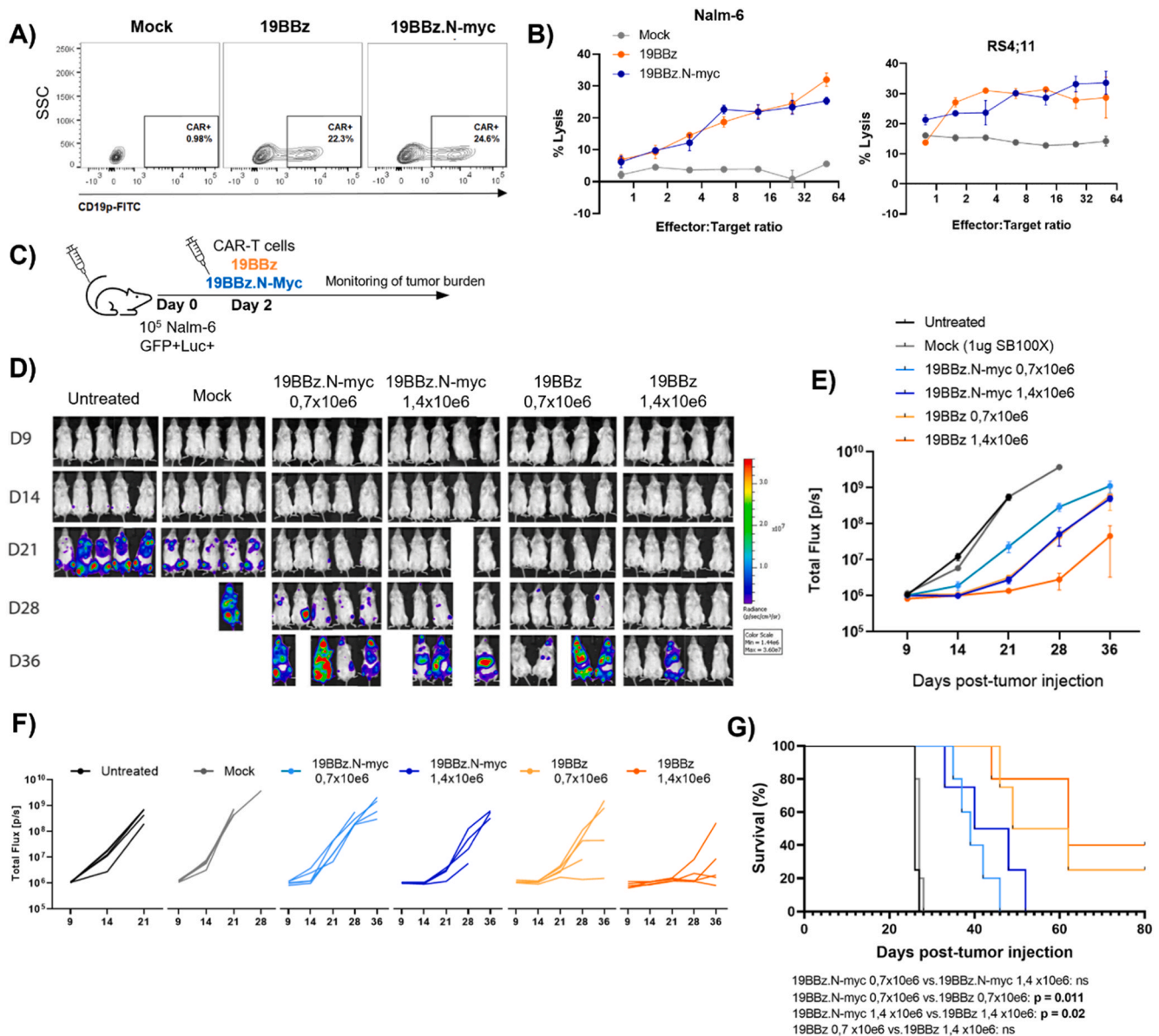
Fig. 5. 19BBz CAR-T cells without the c-Myc tag show higher antitumor efficacy *in vivo*. CAR-T cells were expanded for 8 days and used for cytotoxicity and *in vivo* assay at the end of the expansion. **A)** Percentage of CAR+ cells stained with a FITC-conjugated CD19 protein after 8-day expansion *in vitro*. **B)** 4-hour cytotoxic assay using the same cells depicted in (A) in coculture with CD19 + target cell lines Nalm-6 and RS4;11 in different effector:target ratios. Graph shows mean ± SD of technical triplicates. **C)** Timeline of the *in vivo* experiment. NSG mice were injected with Nalm-6 GFP+Luc+ on day 0 and received treatment on day 2 (Untreated = 5 animals, Mock = 5 animals, 19BBz.N-myc 0.7 $\times 10^6$ = 5 animals, 19BBz.N-myc 1.4 $\times 10^6$ = 4 animals, 19BBz 0.7 $\times 10^6$ = 5 animals, 19BBz 1.4 $\times 10^6$ = 5 animals). **D)** Representative tumor burden images acquired by bioluminescent imaging *in vivo* at different time points. **E)** Total flux quantification of bioluminescent signal showing mean ± SEM and individual animals **(F)**. **G)** Kaplan-Meier survival curve. Survival data was analyzed with the log-rank test.

at the time of euthanasia (Fig. S4 **G**). 19BBz CAR-T cells performed slightly better against CD19lo Nalm-6 than 19BBz.N-myc, although the difference did not reach the significance threshold (Fig. S4 **F**), which could be due to the lower CAR MFI of this donor for the 19BBz condition compared to 19BBz.N-myc (Fig. S4 **B**), a variation found from donor to donor as shown in Fig. 3B. To summarize, these results suggest that the c-Myc tag located in the N-terminus position of the anti-CD19 scFv can interfere with CAR-T cell efficacy *in vivo*.

3.7. The impact of c-Myc tag attached to the scFv C-terminus on scFv-protein interface formation

Based on previous reports of CAR constructs with C-terminus c-Myc tag addition [24], we decided to further investigate whether this

alternative positioning could have less impact in the scFv-target interaction and in CAR-T cell function. The same IIP analysis between c-Myc and CDRs made for the c-Myc attached to the scFv N-terminus structure (c-Myc-scFv) was made for the c-Myc attached to the scFv C-terminus structure (scFv-c-Myc) to determine if the c-Myc tag position could potentially affect the interaction between scFv and the target molecule. This MD simulation data served to elucidate the role of c-Myc in the interaction with the CD19 target, which can be extrapolated to the CAR interaction. The objective was to obtain an inference of the role of c-Myc tag and insertion positions in scFv in the formation and maintenance of the interface between scFvs and target proteins.

The scFv-c-Myc structure was subjected to 700 ns of MD simulation, and the IIP was calculated and shown in Fig. S5. Through this analysis it was possible to infer that in this position, the tag will not interfere with

the interaction since the IIP profile was close to 0 kcal.mol-1 (Fig. S5A), indicating that most of the time there is no interaction between the c-Myc and the scFv CDRs. The IIP distribution histogram (Fig. S5B) shows that almost 100% of the time (Fig. S5C), the c-Myc tag was far apart from the CDRs, being in conformations that do not hinder the interaction with CD19.

The IIP profiles also reveal that the tag has intense movement along the MD since the IIP is oscillating with a large potential amplitude on both systems (c-Myc-scFv and scFv-c-Myc). The average IIP was - 41.99 ± 38.59 and – 0.93 ± 6.40 kcal.mol-1 for c-Myc attached to the N- and C-terminus, respectively (Table 4). The IIP profiles reveal that this tag, when added at the C-terminus position, does not disturb the scFv-protein interface formation since the average IIP is close to zero for interaction with this scFv (Fig S5), meaning it could potentially interfere less with CAR-T cell activity compared to the N-terminus tag.

3.8. Alternative tag positioning in the C-terminus portion of the CAR also hampers CAR-T cell function

To determine whether alternative tag positioning in the C-terminus position of the CAR construct could bypass the negative effect seen with the N-terminus tag construct, we generated the same 19BBz CAR construct as before, but added the c-Myc tag between the scFv heavy chain and the hinge domain, named 19BBz.C-Myc (Fig. S6A). We compared CAR expression between the 3 constructs using both an anti-FMC63 antibody and anti-myc tag antibody (Fig. S6B-**D**). While the detection with anti-FMC63 was similar for all constructs, the 19BBz.C-Myc CAR could not be detected to the same level as the 19BBz.N-Myc with an anti-Myc antibody, as seen by the significant decrease in MFI (Fig. S6C). This suggests that the structural differences in the molecule might influence anti-Myc antibody binding. As before, we also did not observe significant differences in CAR-T cell memory profile after 8-day expansion between groups (Fig. S6E). We then assessed cytotoxic activity of CAR-T cells with the different constructs *in vitro* using a long lysis assay, in which the T cells are co-cultured with Nalm-6 target cells for up to 96 h (Fig. 6**A**). We observed no significant difference between constructs, however, to our surprise, there was a trend towards worse cytotoxic activity of 19BBz.C-Myc CAR-T cells compared to both 19BBz and 19BBz.N-Myc in 2 out of 3 donors. To determine the antitumor activity *in vivo*, we injected 1.5×10^6 CAR+ cells from each construct into Nalm-6 GFP+Luc+ tumor-bearing mice (Fig. 6**B**). Consistently with the lysis assay, we observed significantly impaired antitumor response of 19BBz.C-Myc CAR-T cells compared to 19BBz, and even a slight disadvantage compared to 19BBz.N-Myc CAR-T cells in terms of mice survival (Fig. 6**C**) and tumor load at day 15 post-injection (Fig. 6**D**).

One possible explanation would be that the c-Myc tag in the C-terminus position can influence other regions of the CAR, and this could lead to hampered signaling. The hinge region is one of the logical candidates to be potentially influenced since it is closely connected to the tag in this case. We again used MD simulation, but this time of the CAR structure (extracellular and transmembrane domains) with the c-Myc tag added to the scFv C-terminus. The CAR-C-Myc system was subjected to 400 ns MD simulation, and a distance analysis was made to observe if the c-Myc movements interfered with the hinge structure. The distance analysis was made between the first and last Cα atoms of the c-Myc (Glu243 and Leu262, respectively) (Fig. S7A) to determine whether these atoms came closer during the simulation, which would be indicated by a decrease in the distance value between them. Indeed, we

observed that between 225 ns and 275 ns there was a decrease in distance from 4 nm to 1 nm, demonstrating an approximation and greater packing of the tag (Fig. S8A). The same distance analysis was made for the first and the last Cα atoms of the hinge (Thr263 and Asp307, respectively) (Fig. S7B), indicating that at the same time, between 225 ns and 275 ns, the average distance of 3 nm presented throughout the simulation increased, reaching values of 6 nm, demonstrating that these atoms had moved further apart, that is, that the hinge structure had stretched (Fig. S8B). Overall, it is possible that the C-terminus c-Myc tag can influence other regions of the CAR molecule which potentially also impacts CAR-T cell antitumor activity.

4. Discussion

As CAR-T cell applications advance, novel CAR designs are being developed rapidly and it is expected to be a surge in CAR-T cell pre-clinical studies and clinical trials in the coming years [61]. Reliable CAR detection presents a challenge in the field due to the lack of a universal fast, sensitive, and cost-effective detection method.

Some of the available tools are anti-Fab antibodies and Protein L, which are cost-effective and can be used for different CAR constructs [11]. However, as these reagents target indistinct IgG-like fragments, higher background staining is expected. Additionally, IgG targeting reagents cannot be used to trace CAR constructs with non-scFv extracellular domains. Because of the lack of specific antibodies for each newly developed CAR structure, peptide tags are among the most widely used reporter in basic and applied research with CARs, because of their ease of use and broad applicability [62].

Our MD simulations demonstrated, through RMSD analysis, that the c-Myc presence does not affect the structural equilibrium of the scFv. Moreover, this tag confers greater stability to the scFv, seeing that the structural balance of this protein was reached earlier and the RMSD profile showed smaller fluctuations. This occurs because this tag is associated with the N-terminus of the scFv, which can restrict the movement of this protein. This characteristic of not interfering with the structure and stability of the protein to which the c-Myc tag is associated is due to the particulars of this polypeptide marker, which are seen as advantageous, such as its small size and linear structure [63].

However, MD simulation of the scFv with c-Myc tag in the N-terminus addition indicates, through IIP analysis, that the approximation of c-Myc to the CDRs is ratified or proven by the negative IIP values, and this, in some moments, causes a steric impediment that could disturb the interface formation between the scFv and the CD19 protein. Although the c-Myc tag presence does not affect the structural balance of the scFv, it may reduce the probability of antigen binding. The interaction inhibition of the recombinant protein of interest with its target is one of the main disadvantages resulting from tag addition to these molecules [64], and this disadvantage was observed for the c-Myc tag, when added to the scFv N-terminus, in this study in some MD simulation moments.

Additionally, it was possible to see that when the c-Myc tag was added to the scFv C-terminus, the IIP between c-Myc tag and CDRs was close to 0 kcal.mol^{-1}, indicating that the tag presence would not interfere with the interface formation. Thus, when the Myc tag is added to the scFv N-terminus, it can potentially make interface formation more difficult than when added to the C-terminus. On the other hand, in favorable conformations of the c-Myc tag, even when added to the scFv N-terminus, interface formation between scFv and CD19 is possible, and the maintenance of the interaction throughout the simulation. More negative IIP values between scFv and CD19 were observed in the system with the c-Myc tag (c-Myc-scFv), suggesting that there may be a difference in affinity in this interaction due to the presence of this tag, which was confirmed by the ΔG_{bind} more negative values.

Our results *in vivo* with the Nalm-6 B-ALL xenograft model support the hypothesis of the c-Myc tag interference with CAR-T cell effector function, as we saw decreased antitumor responses in the presence of the tag in both N-terminus and C-terminus positions in different

Table 4
Average IIP and deviations in kcal.mol^{-1} calculated for the interaction between the c-Myc tag and the scFv CDRs.

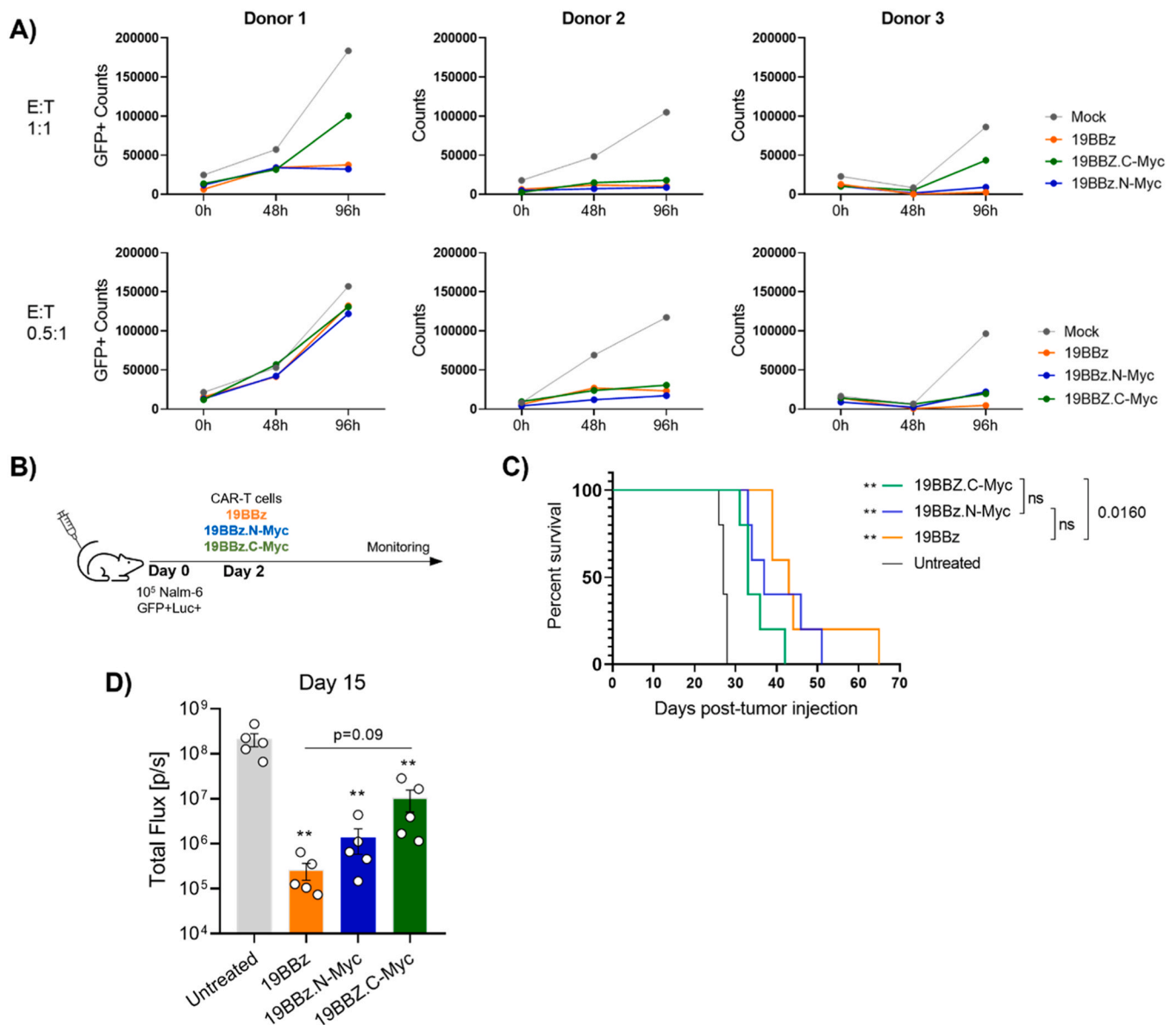| Tag position to scFv	Structure	IIP (kcal.mol^{-1})
N-terminus	c-Myc-CDRs	- 41.99 ± 38.59
C-terminus	CDRs-c-Myc	-0.93 ± 6.40

Fig. 6. *In vitro* and *in vivo* comparison of CAR-T cells containing N- or C-terminus c-Myc tag. **A)** Lysis assay in 1:1 and 0.5:1 effector: target ratio assessed at baseline, 48 and 96 h of coculture with Nalm-6 GFP+ tumor cells. The Y axis shows live target cell count at each timepoint. N = 3 independent donors. **B)** Timeline of *in vivo* experiment. **C)** Survival curve of tumor-bearing mice untreated, or treated with 19BBz, 19BBz.N-Myc or 19BBz.C-Myc CAR-T cells. N = 5 mice/group. **D)** Tumor load was assessed on day 15 post-tumor injection (mean ± SEM).

experiments. Although both CAR-T cells with or without the c-Myc tag addition had significant antitumor response regardless of tag positioning, 19BBz CAR-T cells showed overall slightly superior antitumor capacity compared to both 19BBz.N-Myc and 19BBz.C-myc. Additionally, our CAR-T cell expansion protocol is independent of the CD19 target, so it is possible that using CD19-based expansion protocols (e.g with feeder cells) would reveal an even further impact of the tag presence.

Therefore, even though it has been demonstrated *in silico* that the c-Myc presence at the C-terminus of the scFv does not interfere with the interface formation between the scFv and its target, in this study, we found that in this position the intrinsic movement of the tag can interfere with the hinge structure (Fig. S7 and S8), which potentially interferes with CAR activity as well. It is known that the hinge plays an important role in the surface expression level, in the efficiency of membrane transport, and in defining the signaling threshold of the CAR [65].

In conclusion, our results suggest that peptide tags should be used

carefully to avoid their presence affecting CAR function and interaction with the target molecule. Other reporters that are not directly linked to the CAR molecule, such as fluorescent molecules or membrane reporters like dNGFR might be suitable alternatives, although they might pose different challenges [28,29]. Finally, it should be taken into consideration when moving from pre-clinical to clinical research (where the CAR design usually does not include epitope tags) that the same CAR design without a peptide tag might have more potent activity than previously expected.

4.1. Limitations of the study

We are aware that the results presented in this work may vary for different scFv-target pairs, as our study focused on the FMC63-based 19BBz CAR and the CD19 protein, the scFv CAR/target molecule most widely used in the clinical setting. In our study design, we opted for directly assessing impact of tag addition on CAR-T cell efficacy *in vivo*,

but we recognize that *in vitro* biochemical binding assays comparing different tags and their positioning are most valuable to further tackle the question of which tag and which position have the least potential to interfere with CAR-target recognition.

CRediT authorship contribution statement

Emmanuel Arthur Albuquerque Aragão: Data curation, Formal analysis, Writing – review & editing. **Clara de Oliveira Andrade:** Data curation, Formal analysis, Writing – review & editing. **Eduardo Mannarino Correia:** Data curation, Formal analysis, Writing – review & editing. **Leonardo Ribeiro Batista-Silva:** Data curation, Writing – review & editing. **Luiza Abdo:** Data curation, Formal analysis, Writing – review & editing. **Marcos Roberto Lourenzoni:** Conceptualization, Funding acquisition, Supervision, Writing – review & editing. **Martín Hernan Bonamino:** Conceptualization, Funding acquisition, Supervision, Writing – review & editing. **Karina Lobo Hajdu:** Data curation, Formal analysis, Writing – original draft, Writing – review & editing. **Ana Julia Ferreira Lima:** Data curation, Formal analysis, Writing – original draft, Writing – review & editing.

Declaration of Competing Interest

None.

Appendix A. Supporting information

Supplementary data associated with this article can be found in the online version at doi:10.1016/j.csbj.2024.05.032.

References

[1] Benmebarek MR, Karches CH, Cadilha BL, Lesch S, Endres S, Kobold S. Killing mechanisms of chimeric antigen receptor (CAR) T cells. Int J Mol Sci 2019;20(6): 1283. https://doi.org/10.3390/ijms20061283.

[2] Larson RC, Maus MV. Recent advances and discoveries in the mechanisms and functions of CAR T cells. Nat Rev Cancer 2021;21(3):145–61. https://doi.org/10.1038/s41568-020-00323-z.

[3] Stoiber S, Cadilha BL, Benmebarek MR, Lesch S, Endres S, Kobold S. Limitations in the design of chimeric antigen receptors for cancer therapy. Cells 2019;8(5):472. https://doi.org/10.3390/cells8050472.

[4] Lindner SE, Johnson SM, Brown CE, Wang LD. Chimeric antigen receptor signaling: functional consequences and design implications. Sci Adv 2020;6(21):eaaz3223. https://doi.org/10.1126/sciadv.aaz3223.

[5] Abdo L, Aragão EA, Bonamino M. Structural determinants of chimeric antigen receptor design. Crit Rev Immunol 2021;41(1):89–104. https://doi.org/10.1615/CritRevImmunol.2021037551.

[6] Chicaybam L, Bonamino MH, Luckow Invitti A, Bortman Rozenchan P, de Luna Vieira I, Strauss BE. Overhauling CAR T cells to improve efficacy, safety and cost. Cancers 2020;12(9):2360. https://doi.org/10.3390/cancers12092360.

[7] U.S. Food and Drug Administration. KYMRIAH (tisagenlecleucel). Available online: https://www.fda.gov/biologicsbloodvaccines/cellulargenetherapyproducts/approvedproducts/ucm573706.htm (accessed on 20 November 2022).

[8] U.S. Food and Drug Administration. YESCARTA (axicabtagene ciloleucel). Available online: https://www.fda.gov/biologicsbloodvaccines/cellulargenetherapyproducts/approvedproducts/ucm581222.htm (accessed on 20 November 2022).

[9] Forsberg MH, Das A, Saha K, Capitini CM. The potential of CAR T therapy for relapsed or refractory pediatric and young adult B-cell ALL. Ther Clin risk Manag 2018;14:1573–84. https://doi.org/10.2147/TCRM.S146309.

[10] Mazzi MT, Hajdu KL, Ribeiro PR, Bonamino MH. CAR-T cells leave the comfort zone: current and future applications beyond cancer. Immunother Adv 2020;1(1): ltaa006. https://doi.org/10.1093/immadv/ltaa006.

[11] Gopalakrishnan R, Matta H, Choi S, Natarajan V, Prins R, Gong S, et al. A novel luciferase-based assay for the detection of Chimeric Antigen Receptors. Sci Rep 2019;9(1):1957. https://doi.org/10.1038/s41598-018-38258-z.

[12] Jena B, Maiti S, Huls H, Singh H, Lee DA, Champlin RE, et al. Chimeric antigen receptor (CAR)-specific monoclonal antibody to detect CD19-specific T cells in clinical trials. PloS One 2013;8(3):e57838. https://doi.org/10.1371/journal.pone.0057838.

[13] Zheng Z, Chinnasamy N, Morgan RA. Protein L: a novel reagent for the detection of chimeric antigen receptor (CAR) expression by flow cytometry. J Transl Med 2012; 10:29. https://doi.org/10.1186/1479-5876-10-29.

[14] De Oliveira SN, Wang J, Ryan C, Morrison SL, Kohn DB, Hollis RP. A CD19/Fc fusion protein for detection of anti-CD19 chimeric antigen receptors. J Transl Med 2013;11:23. https://doi.org/10.1186/1479-5876-11-23.

[15] Schüchner S, Behm C, Mudrak I, Ogris E. The Myc tag monoclonal antibody 9E10 displays highly variable epitope recognition dependent on neighboring sequence context. Sci Signal 2020;13(616):eaax9730. https://doi.org/10.1126/scisignal.aax9730.

[16] Lichty JJ, Malecki JL, Agnew HD, Michelson-Horowitz DJ, Tan S. Comparison of affinity tags for protein purification. Protein Expr Purif 2005;41(1):98–105. https://doi.org/10.1016/j.pep.2005.01.019.

[17] Terpe K. Overview of tag protein fusions: from molecular and biochemical fundamentals to commercial systems. Appl Microbiol Biotechnol 2003;60(5): 523–33. https://doi.org/10.1007/s00253-002-1158-6.

[18] Wood DW. New trends and affinity tag designs for recombinant protein purification. Curr Opin Struct Biol 2014;26:54–61. https://doi.org/10.1016/j.sbi.2014.04.006.

[19] Kimple ME, Brill AL, Pasker RL. Overview of affinity tags for protein purification. 9.9.1–9.9.23 Curr Protoc Protein Sci 2013;73. https://doi.org/10.1002/0471140864.ps0909s73.

[20] Chicaybam L, Abdo L, Viegas M, Marques LVC, de Sousa P, Batista-Silva LR, et al. Transposon-mediated generation of CAR-T cells shows efficient anti B-cell leukemia response after ex vivo expansion. Gene Ther. 2020;27(1-2):85–95. https://doi.org/10.1038/s41434-020-0121-4.

[21] Evan GI, Lewis GK, Ramsay G, Bishop JM. Isolation of monoclonal antibodies specific for human c-myc proto-oncogene product. Mol Cell Biol 1985;5(12): 3610–6. https://doi.org/10.1128/mcb.5.12.3610-3616.1985.

[22] Mahmoudi Gomari M, Saraygord-Afshari N, Farsimadan M, Rostami N, Aghamiri S, Farajollahi MM. Opportunities and challenges of the tag-assisted protein purification techniques: applications in the pharmaceutical industry. Biotechnol Adv 2020;45:107653. https://doi.org/10.1016/j.biotechadv.2020.107653.

[23] Nunoya JI, Masuda M, Ye C, Su L. Chimeric antigen receptor T cell bearing herpes virus entry mediator co-stimulatory signal domain exhibits high functional potency. Mol Ther Oncol. 2019;14:27–37. https://doi.org/10.1016/j.omto.2019.03.002.

[24] Li W, Qiu S, Chen J, Jiang S, Chen W, Jiang J, et al. Chimeric antigen receptor designed to prevent ubiquitination and downregulation showed durable antitumor efficacy. Immunity 2020;53(2):456–470.e6. https://doi.org/10.1016/j.immuni.2020.07.011.

[25] Muller YD, Nguyen DP, Ferreira LMR, Ho P, Raffin C, Valencia RVB, et al. The CD28-transmembrane domain mediates chimeric antigen receptor heterodimerization with CD28. Front Immunol 2021;12:639818. https://doi.org/10.3389/fimmu.2021.639818.

[26] Karplus M, McCammon JA. Molecular dynamics simulations of biomolecules. Nat Struct Biol 2002;9(9):646–52. https://doi.org/10.1038/nsb0902-646.

[27] van Gunsteren WF, Dolenc J, Mark AE. Molecular simulation as an aid to experimentalists. Curr Opin Struct Biol 2008;18(2):149–53. https://doi.org/10.1016/j.sbi.2007.12.007.

[28] Chen J, López-Moyado IF, Seo H, Lio CJ, Hempleman LJ, Sekiya T, et al. NR4A transcription factors limit CAR T cell function in solid tumours. Nature 2019;567 (7749):530–4. https://doi.org/10.1038/s41586-019-0985-x.

[29] Iwamoto N, Patel B, Song K, Mason R, Bolivar-Wagers S, Bergamaschi C, et al. Evaluation of chimeric antigen receptor T cell therapy in non-human primates infected with SHIV or SIV. PloS One 2021;16(3):e0248973. https://doi.org/10.1371/journal.pone.0248973.

[30] Webb B, Sali A. Comparative Protein Structure Modeling Using MODELLER. 5.6.1–5.6.37 Curr Protoc Bioinforma 2016;54. https://doi.org/10.1002/cpbi.3.

[31] Shen MY, Sali A. Statistical potential for assessment and prediction of protein structures. Protein Sci: a Publ Protein Soc 2006;15(11):2507–24. https://doi.org/10.1110/ps.062416606.

[32] The PyMOL Molecular Graphics System, Version 1.8 Schrödinger, LLC.

[33] van Zundert GCP, Rodrigues JPGLM, Trellet M, Schmitz C, Kastritis PL, Karaca E, Melquiond ASJ, van Dijk M, de Vries SJ, Bonvin AMJJ. The HADDOCK2.2 web server: user-friendly integrative modeling of biomolecular complexes. J Mol Biol 2016;428(4):720–5. https://doi.org/10.1016/j.jmb.2015.09.014.

[34] Dominguez C, Boelens R, Bonvin AM. HADDOCK: a protein-protein docking approach based on biochemical or biophysical information. J Am Chem Soc 2003;125(7):1731–7. https://doi.org/10.1021/ja026939x.

[35] Melquiond, A.S.J. & Bonvin, A.M.J.J. (2010). Data-driven docking: using external information to spark the biomolecular rendez-vous. In: Protein-protein complexes: analysis, modelling and drug design. Edited by M. Zacharrias, Imperial College Press, 183–209. https://doi.org/10.1142/9781848163409_0007.

[36] Ghorashian S, Kramer AM, Onuoha S, Wright G, Bartram J, Richardson R, et al. Enhanced CAR T cell expansion and prolonged persistence in pediatric patients with ALL treated with a low-affinity CD19 CAR. Nat Med 2019;25(9):1408–14. https://doi.org/10.1038/s41591-019-0549-5.

[37] Klesmith JR, Wu L, Lobb RR, Rennert PD, Hackel BJ. Fine epitope mapping of the CD19 extracellular domain promotes design. Biochemistry 2019;58:4869–81. https://doi.org/10.1021/acs.biochem.9b00808.

[38] He C, Mansilla-Soto J, Khanra N, Hamieh M, Bustos V, Paquette AJ, et al. CD19 CAR antigen engagement mechanisms and affinity tuning. Sci Immunol 2023;8 (81):eadf1426. https://doi.org/10.1126/sciimmunol.adf1426.

[39] Abraham MJ, Murtola T, Schulz R, Páll S, Smith JC, Hess B, et al. GROMACS: high performance molecular simulations through multi-level parallelism from laptops to supercomputers. SoftwareX 2015;1:19–25. https://doi.org/10.1016/j.softx.2015.06.001.

[40] Huang J, MacKerell Jr AD. CHARMM36 all-atom additive protein force field: validation based on comparison to NMR data. J Comput Chem 2013;34(25):2135–45. https://doi.org/10.1002/jcc.23354.

[41] Anandakrishnan R, Aguilar B, Onufriev AV. H++ 3.0: automating pK prediction and the preparation of biomolecular structures for atomistic molecular modeling and simulations. Nucleic Acids Res 2012;40(Web Server issue):W537–41. https://doi.org/10.1093/nar/gks375.

[42] Jorgensen WL, Chandrasekhar J, Madura JD, Impey RW, Klein ML. Comparison of simple potential functions for simulating liquidWater. J Chem Phys 1983;79:926–35. https://doi.org/10.1063/1.445869.

[43] Hess B. P-LINCS: a parallel linear constraint solver for molecular simulation. J Chem Theory Comput 2008;4(1):116–22. https://doi.org/10.1021/ct700200b.

[44] Hess B, Bekker H, Berendsen HJC. LINCS: a linear constraint solver for molecular simulations. J Comput Chem 1997;18:1463–72. https://doi.org/10.1002/(SICI)1096-987X(199709)18:12<1463::AID-JCC4>3.0.CO;2-H.

[45] van Gunsteren WF, Berendsen HJC. Algorithms for macromolecular dynamics and constraint dynamics. Mol Phys 1977;34:1311–27. https://doi.org/10.1080/00268977700102571.

[46] Essmann U, Perera L, Berkowitz ML, Darden T, Lee H, Pedersen LG. A smooth particle mesh ewald method. J Chem Phys 1995;103:8577–93. https://doi.org/10.1063/1.470117.

[47] Haug EJ, Arora JS, Matsui K. A steepest-descent method for optimization of mechanical systems. J Optim Theory Appl 1976;19:401–24. https://doi.org/10.1007/BF00941484.

[48] Bussi G, Donadio D, Parrinello M. Canonical sampling through velocity rescaling. J Chem Phys 2007;126(1):014101. https://doi.org/10.1063/1.2408420.

[49] Berendsen HJC, Postma JPM, van Gunsteren WF, DiNola A, Haak JR. Molecular dynamics with coupling to an external bath. J Chem Phys 1984;81:3684–90. https://doi.org/10.1063/1.448118.

[50] Parrinello M, Rahman A. Crystal structure and pair potentials: a molecular dynamics study. Am Phys Soc 1980;45:1196–9. https://doi.org/10.1103/PhysRevLett.45.1196.

[51] Hockney R, Goel S, Eastwood J. Quiet high-resolution computer models of a plasma. J Comput Phys 1974;14:148–58. https://doi.org/10.1016/0021-9991(74)90010-2.

[52] Jo S, Kim T, Iyer VG, Im W. CHARMM-GUI: a web-based graphical user interface for CHARMM. J Comput Chem 2008;29(11):1859–65. https://doi.org/10.1002/jcc.20945.

[53] Bougnoux P, Salem N, Lyons C, Hoffman T. Alteration in the membrane fatty acid composition of human lymphocytes and cultured transformed cells induced by interferon. Mol Immunol 1985;22(9):1107–13. https://doi.org/10.1016/0161-5890(85)90114-2.

[54] Kumari, R., Kumar, R., Open Source Drug Discovery Consortium, & Lynn, A. (2014). g_mmpbsa–a GROMACS tool for high-throughput MM-PBSA calculations. Journal of chemical information and modeling, 54(7), 1951–1962. https://doi.org/10.1021/ci500020m.

[55] Imai C, Mihara K, Andreansky M, Nicholson IC, Pui CH, Geiger TL, et al. Chimeric receptors with 4-1BB signaling capacity provoke potent cytotoxicity against acute lymphoblastic leukemia. Leukemia 2004;18(4):676–84. https://doi.org/10.1038/sj.leu.2403302.

[56] Nicholson IC, Lenton KA, Little DJ, Decorso T, Lee FT, Scott AM, et al. Construction and characterisation of a functional CD19 specific single chain Fv fragment for immunotherapy of B lineage leukaemia and lymphoma. Mol Immunol 1997;34(16-17):1157–65. https://doi.org/10.1016/s0161-5890(97)00144-2.

[57] Mátés L, Chuah MK, Belay E, Jerchow B, Manoj N, Acosta-Sanchez A, et al. Molecular evolution of a novel hyperactive Sleeping Beauty transposase enables robust stable gene transfer in vertebrates. Nat Genet 2009;41(6):753–61. https://doi.org/10.1038/ng.343.

[58] Chicaybam L, Sodre AL, Curzio BA, Bonamino MH. An efficient low cost method for gene transfer to T lymphocytes. PLoS One 2013;8(3):e60298. https://doi.org/10.1371/journal.pone.0060298.

[59] Neri S, Mariani E, Meneghetti A, Cattini L, Facchini A. Calcein-acetyoxymethyl cytotoxicity assay: standardization of a method allowing additional analyses on recovered effector cells and supernatants. Clin Diagn Lab Immunol 2001;8(6):1131–5. https://doi.org/10.1128/CDLI.8.6.1131-1135.2001.

[60] Kufareva I, Abagyan R. Methods of protein structure comparison. Methods Mol Biol (Clifton, N J) 2012;857:231–57. https://doi.org/10.1007/978-1-61779-588-6_10.

[61] Maryamchik E, Gallagher KME, Preffer FI, Kadauke S, Maus MV. New directions in chimeric antigen receptor T cell [CAR-T] therapy and related flow cytometry. Cytom Part B, Clin Cytom 2020;98(4):299–327. https://doi.org/10.1002/cyto.b.21880.

[62] Gong Y, Klein Wolterink RGJ, Wang J, et al. Chimeric antigen receptor natural killer (CAR-NK) cell design and engineering for cancer therapy. J Hematol Oncol 2021;14:73. https://doi.org/10.1186/s13045-021-01083-5.

[63] Zhao X, Li G, Liang S. Several affinity tags commonly used in chromatographic purification. J Anal Methods Chem 2013;2013:581093. https://doi.org/10.1155/2013/581093.

[64] Majorek KA, Kuhn ML, Chruszcz M, Anderson WF, Minor W. Double trouble-Buffer selection and His-tag presence may be responsible for nonreproducibility of biomedical experiments. Protein Sci: a Publ Protein Soc 2014;23(10):1359–68. https://doi.org/10.1002/pro.2520.

[65] Fujiwara K, Tsunei A, Kusabuka H, Ogaki E, Tachibana M, Okada N. Hinge and transmembrane domains of chimeric antigen receptor regulate receptor expression and signaling threshold. Cells 2020;9(5):1182. https://doi.org/10.3390/cells9051182.